MTLA 34 (2024) 102088

Contents lists available at ScienceDirect

Materialia

journal homepage: www.elsevier.com/locate/mtla

Development of 3D printed tissue-mimicking materials: Combining fiber reinforcement and fluid content for improved surgical rehearsal

Othniel James Aryeetey [a,b], Laszlo Jaksa [a,c], Martin Bittner-Frank [b], Andrea Lorenz [c], Dieter H. Pahr [a,b,*]

[a] TU Wien, Institute of Lightweight Design and Structural Biomechanics, Gumpendorfer Straße 7, 1060 Vienna, Austria
[b] Karl Landsteiner University of Health Sciences, Department of Anatomy and Biomechanics, Division Biomechanics, Dr. Karl-Dorrek-Straße 30, 3500 Krems, Austria
[c] Austrian Center for Medical Innovation & Technology (ACMIT), Viktor Kaplan-Straße 2/1, 2700 Wiener Neustadt, Austria

ARTICLE INFO

Keywords:
Viscoelasticity
Multi-material
Soft tissue
3dprinting

ABSTRACT

The prevalence of medical errors during surgical procedures has led to a higher emphasis on improving surgical outcomes, by improving surgical planning and training. Anatomical models have become valuable tools for pre-operative planning and current 3D printed models strive to better match real soft biological tissues. This study aimed to develop novel 3D printed material composites with controllable mechanical properties that mimic soft tissue. Concepts of microstructuring, fiber reinforcement and fluid infill in extrusion-based 3D printing are combined to design tunable materials towards target tissues of porcine muscle and liver. Material characterization was performed in triangular wave cyclic experiments under uniaxial tension with increasing displacements. Hereby, initial E_I and final E_{II} elastic moduli were evaluated. Further, the viscous response was characterized by the dissipated energy ratio U_D and suture retention strength (SRS) was determined by single tensile pull-out tests Elastic moduli of printed materials were successfully tuned to 510 ± 10 kPa, closely resembling porcine muscle with 580 ± 150 kPa. The dissipated energy ratio U_D of the silicone was increased from 0.09 ± 0.01 to 0.46 ± 0.17 by addition of gyroid infill and viscous fluid. Suture retention strength (SRS) for porcine liver tissue was 1.64 ± 0.42 N, while that of 3D printed silicone showed a mean SRS of 5.1 ± 0.6 N. Although the exact properties of porcine muscle and liver tissue require finer tuning, this study established techniques for refinement of 3D printed tissue-mimicking materials, ultimately enabling more accurate models for surgical rehearsal.

1. Introduction

Recently, it has been suggested that 'medical errors' lead to a mean death rate of about 250,000 patients each year in the United States alone [1]. Hence, a higher emphasis has been placed on reducing patient mortality through improved surgical planning and training. The use of anatomical models in research, teaching and surgical rehearsal has therefore risen significantly in the past few decades [2].

Advancements in medical imaging technology have led to the emergence of higher resolution, non-invasive imaging methods, such as Computed tomography and advanced MRI imaging. Although these techniques are increasingly capable of capturing more intricate details of the anatomical structures within a patient's body, a two-dimensional portrayal of anatomy can obscure the complex spatial relationships between tissues [3]. 3D virtual models help here to visualize organs structures and enhance visualization and communication. However, they lack the tactile feedback necessary for surgical rehearsal and practice. Producing a 3D physical model of an individual's organ can significantly improve this aspect, offering a more tangible approach for medical professionals [4]. The advent of additive manufacturing, commonly referred to as 3D printing, along with improvements in image processing, has enabled complex patient-specific physical anatomical models to be developed [5,6]. The use of these models enables pre-operative key feature identification, implant customization, intra-operative guidance and an improved patient communication [7,8].

3D printed anatomical models have been implemented in many surgical fields [9]. For instance, in neurosurgery, a high degree of accuracy is needed [10]. As such, 3D printed models of a cerebral aneurysm were generated using ABS and photoresins by Scerrati et al. [11] and more recently, a neonatal anatomical model was printed by Wagner et al. [12] using polyjet technology. In other fields, such as in Urology, resin printed prostate tumor models were presented by Shin et al. [13]

* Corresponding author.

https://doi.org/10.1016/j.mtla.2024.102088
Received 13 January 2024; Accepted 9 April 2024
Available online 11 April 2024

and Wang et al. [14]. Anatomical models have made a large impact in cardiology [15–19], pulmonary medicine [20–22], hepatology [23,24] and abdominal surgery [25–27]. Despite the advancements in 3D printing technologies, a common drawback of some of these previously mentioned studies is that the materials tend to be stiffer and less compliant than real soft biological tissue.

This led to the use of softer and more compliant materials such as silicone and hydrogels [28–30], often combining indirect methods such as molding, casting or injection with 3D printing [9]. Models of blood vessels are often created by applying 3D printing to a sacrificial part which is later melted or dissolved to create hollow structures [31,32]. Maddox et al. [33] created 3D printed renal units using a multi-jet 3D printer to form the outer shell of the renal tissue and injected agarose gel solution into the inner cavity of the model to achieve more realistic patient-specific renal malignancies. Ishii et al. [34] created a patient-specific liver model composed of three separate parts by directly 3D printing blood vessels and the shell of the liver and then molding the parenchyma with soft polyurethane resin using a 3D printed mold. The aim of these studies have been primarily to ensure that the mechanical properties of anatomical models are in the same order of magnitude as the target soft tissues. This is a clear trend showing the importance of the tactile response properties of anatomical models for surgical rehearsal. Although these combined direct and indirect methods tend to exhibit an overall more realistic tissue behavior, the mechanical properties of combined casted and 3D printed parts may be difficult to characterize accurately with conventional testing methods. Moreover, in these approaches the material properties are often not easily tunable to better match other use-cases.

Here, we propose a methodology for the creation of anatomical tissue models with tunable and measurable mechanical properties. The approach involves direct 3D printing of two types of silicones in combination with standard fused deposition modeling (FDM) printing. Tissues are printed with a controllable microstructure or 'infill', to tune the material's stiffness and viscous properties. A novel concept was applied to increase the material's viscous response under uniaxial cyclic loading by introducing a fluid silicone oil with high viscosity into the matrix of the designed sample. Additionally, stiff wavy fibres were printed directly into the matrix of the samples to tune the material's elastic response from a linear elastic response to a more non-linear response typical of soft tissue. This study is novel in that it combines fibre reinforcement, microstructuring and fluid infill in extrusion-based 3D printed materials to produce tunable tissue mimicking materials for the creation of anatomically accurate surgical rehearsal models.

2. Methods

2.1. Theory

Target tissues were selected to be porcine liver and porcine muscle as reference mechanical properties and due to the readily availability of these tissues for testing. Hepatic tissue is regarded as being homogenous and isotropic and one of the softer biological tissues [35] and hence served as a lower boundary of target tissues. Muscle tissues have been shown to be in the upper range of soft biological tissue stiffnesses, [36–38] and hence serve as the upper boundary of target tissues.

The main approach employs 3D printable condensation-crosslinking single component (1 K) silicone materials as a base material for the tissue mimicking material (TMM). Addition of microstructuring or infill enables the control of material stiffness [39] and may introduce some viscoelastic responses [40,41]. Elastomers display linear stress strain behaviour in the range of surgical manipulation (10 % to 25 %), whereas soft biological tissues have a non-linear stress strain relationship [42]. Hence, a technique to introduce the strain softening behaviour of soft biological tissue into linear elastic polymer is the inclusion of wavy fibre reinforcement in the matrix of the material, as seen in previous literature [43,44]. This creates a controlled mismatch, such that the material stiffness is dominated at lower strains by the matrix and higher strains by the fibres [45,46]. Soft biological tissues have been shown to have higher energy absorption.i.e. larger hysteresis under cyclic loading [47, 48] as compared to elastomers. Here, novel approach was developed to include silicone oil as a filler fluid is employed to increase the elastomers viscosity. In total, four major specimen groups were created and tested: Soft biological tissue, base silicones, i.e., with unaltered material properties, fibred samples and tuned samples. Three samples per specimen group were tested for repeatability and mean results with standard deviation are reported.

2.1.1. Elastic stiffness tuning

Elastic tuning to change the non-linear elastic behaviour of the samples was performed by incorporating stiffening fibres into the silicon matrix. Wang et al. [45,42] as well as by Garcia et al. [46] showed that the non-linear response of base polymeric materials can be tuned to achieve strain stiffening behaviour by embedding stiff wavy fibres in the soft polymeric material, given that these structures have the right design parameters. During loading the stiffer wave fibres are engaged once fully stretched and produce an increase in stiffness at a given strain range. This inflection region is characteristic of a given soft tissue that mimics the effect of collagen fibres within the soft tissue [49]. The increase in stiffness is dependent on the stiffness of the fibre, while the inflection region is based on the wavelength of the embedded fibres. In order to reduce the general stiffness of the material, the study focused on both the initial E_I and final E_{II} elastic moduli. The overall stiffness was lowered by introducing an infill pattern whilst printing, also reducing the overall material mass.

2.1.2. Viscous behaviour tuning

It has been shown that an increase in fluid content in soft biological tissue corresponds to a faster rate of relaxation and hence an increase in the dissipated energy [50,51]. Viscous tuning aims to increase the energy dissipation by the tissue mimicking material under cyclic loading. To achieve this, a high viscous fluid, PDMS oil, is introduced to the polymeric matrix to introduce a dampening effect.

2.1.3. Suture retention test

The suture retention strength (SRS) as defined by the AAMI/ISO/ANSI 7198 Standard (2016) as the anastomotic strength or "the force necessary to pull a suture from a prosthesis or cause failure in the wall of a prosthesis". Here we apply the same definition to tissue. Mine et al. [52] showed that, depending on the breakage pattern for a biological tissue, a break starts much earlier than the maximum suture retention strength (SRS), this is referred to as the breaking start strength (BSS). The influence of the test design has been shown to also have a marked effect on the results of the suture retention test and hence test parameters were chosen with special care considering the effect of suture bite size [53], location and suture size [54] and clamping [55]. BSS and SRS of porcine liver tissue and a 3D printed sample were assed in the current study.

2.2. Sample preparation

2.2.1. Multi-material 3D printer

Samples were created using a custom-made multi-material 3D printer capable of printing two highly viscous fluids as well as a filament extrusion. The printer was developed using a modified Railcore II 300 ZL open-source 3D printer system with an extrusion-based extruder printhead composed of a Vipro-HEAD 3/3 two-component printhead (Viscotec GmbH, Toging am Inn, Germany). This enables processing two single-component silicones, or a two-component silicone in combination with a standard E3D V6 FFF printhead for depositing thermoplastic filaments (see Fig. 1). A customized printing nozzle was designed to enable the use of various printer nozzle diameters.

The silicone printing nozzle is connected to the outlet of the extruder

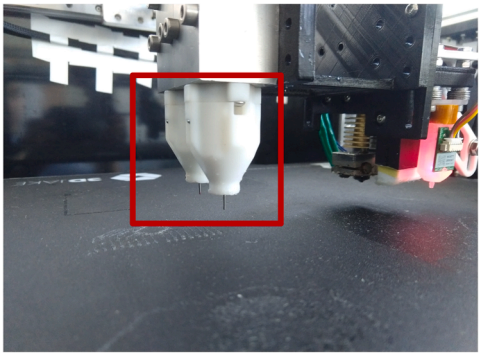

Fig. 1. Custom-made multi-material 3D printer with a 2 component ViproHead printhead (Viscotec GmbH, Toeging am Inn, Germany) capable of printing in combination with a standard E3D V6 FFF printhead.

through a Luer-thread and is secured against unscrewing with a retainer part. These white Luer-adapters and retainers were custom-made for the extruder. A nozzle with 0.4 mm outlet diameter was selected for silicone extrusion. The original E3D V6 FFF printhead on the other side of the carriage is capable of melting and depositing thermoplastic filaments through a 0.4 mm diameter nozzle (see Fig. 1). Accuracy of the 3D printed models was considered in terms of recommendation made in previous publication by Jaksa et al. [56,57] with regards to aspects such as recommended wall thickness, slenderness ratios, bridging lengths and overhang angles.

2.2.2. Materials

To create tissue mimicking specimens, three main material components were required. A 3D printable base material, a stiffening material component to mimic the strain stiffening effect of soft biological tissue, and a viscous fluid-like component for the tuning of viscoelastic mechanical properties.

Four single-component high viscosity, condensation-crosslinking liquid silicone rubber Elkem AMSil20101, AMSil20102, AMSil20103, AMSil20104 (Elkem Silicones SAS, Lyon, France) were tested for use as a base matrix. The selection was made primarily based on the ease of printability and curing of the material as well as the Elastic moduli of the silicones. To enable elastic tuning, two printable stiffer material components were tested. A standard polylactic Acid (PLA) fibre (Material4Print GmbH & co. KG, Loehne, Germany) and a more flexible

Thermoplastic Urethane (TPU) filament, Varioshore Natural (ColorFabb B.V. Belfeld, Netherlands), each filament with a standard 1.75

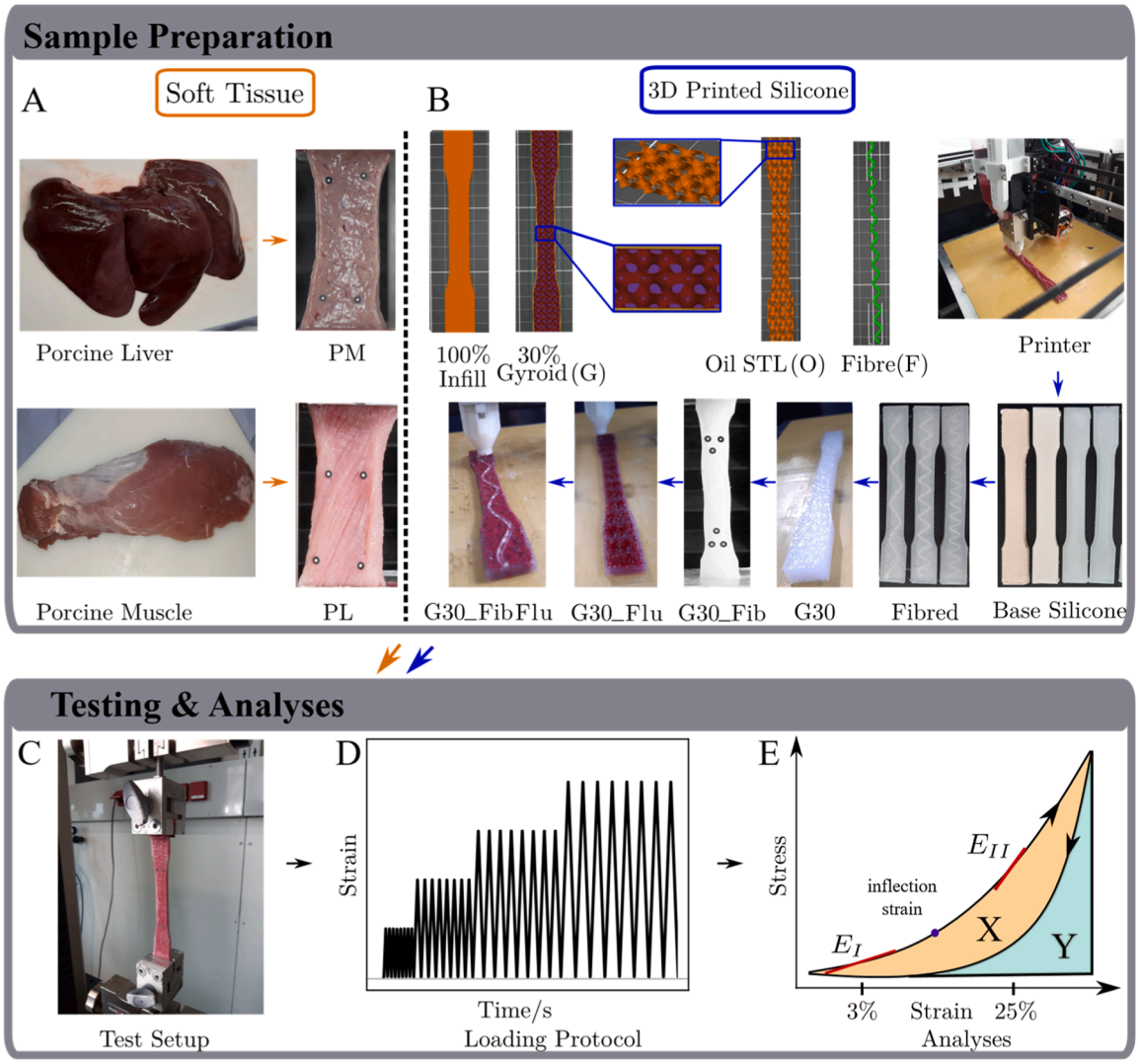

Fig. 2. Flow chart showing the methodology of the study. A) Soft tissue section shows sample preparation of porcine muscle and liver tissue. B) 3D printed section shows the creation of tissue mimicking 3D printed silicone samples from design, printing to final samples. C) mechanical test setup. D) cyclic loading protocol. E) analyzed parameters, initial E_I and final E_{II} Elastic moduli,inflection strain ε_i as well as energy areas (X,Y).

mm diameter. The latter was printed at 210 °C to activate the foaming expansion to decrease the fibre stiffness. For viscous tuning, a high dynamic viscosity (100 Pas) Polydimethylsiloxane (PDMS) oil (Optimal Products GmbH, Bad Oeynhausen, Germany) was selected as a fluid filler material. Additionally, the PDMS oil was mixed with 1 w/w% Silc Pig "Blood" paint (Smooth-On Inc., Macungie, PE). It was assumed that this coloring additive does not have a significant effect on the overall mechanical behavior of the PDMS oil, due to negligible weight amount. It was hypothesized that the fluid like nature as well as the inherent viscosity of the PDMS Oil would significantly increase the overall viscous response of the designed material.

2.2.3. Sample design

In this study, soft biological tissues, porcine muscle and liver tissue were prepared into rectangular shape 70 mm x 20 mm x 5 mm thick samples as previously described in [34] for cyclic uniaxial testing (see Fig. 2A). Initial tests were conducted on base silicone materials (Elk01, Elk02, Elk03, Elk04) as well as fibre reinforced samples (Elk01LF, Elk01MF, Elk01HF) using Type I dogbone samples in accordance with ASTM Standard D638–14 as shown in Fig. 2B.

Tuned concept specimens (G30, G30Fib, G30Flu, G30FibFlu) were designed based on the results of preliminary tests (see Table 1 for a description of all designed samples). In order to create cavities for the fluid infill, and prevent fluid loss during testing, the samples required an outer wall thickness of at least 1 mm. To mitigate the effect of thickened walls on the test results, the sample design was increased in width and thickness to 10 mm and 14 mm respectively, with a gauge length of 70 mm (see Fig. 2B).

Tuned samples were created with gyroid infill structures using parametric CAD design tools, specifically Rhinoceros 7 (Robert Mcneel & Associates, Seattle USA) with the Grasshopper™, and Crystallon plugins. A basic CAD design of the dogbone sample was created in the Rhinoceros CAD design environment and shelled to a thickness of 1.2 mm. The shell thickness defines the thickness of the printed wall. Using the Crystallon Plugin, the obtained cavity within the shelled CAD object was filled with a gyroid structure, the minimum thickness of each gyroid was the print head nozzle diameter (0.4 mm) plus a tolerance of 0.1 mm i.e. (0.5 mm). The gyroids were patterned in x, y and z directions such that they filled a 30 % volume of the CAD dogbone model, based on comparisons to Prusa Slicer infill volumes. A boolean operation was carried out to ensure that the internal gyroid structure conformed to the internal volume of the dogbone structure and outliers were removed. The internal cavity was then copied, to give an additional dogbone model with internal dimensions of the shelled CAD model. The internal dogbone was boolean subtracted by the fitted internal gyroid structure to produce the negative volume which would serve as the negative space for fluid infill. The stiff wavy fibres were produced by a simple sinusoidal wave function line in Rhinoceros 7 plugin Grasshopper. A pipe function was applied to the line with a radius of 0.9 mm. Fibre structures were designed based on literature studies by Wang et al. [42,45], which showed that a sinusoidal wave embedded in a soft polymeric material with a selected wavelength introduced strain stiffening behaviour. Three main design parameters were considered, the wavelength of the fibre λ, the amplitude A and the radius of the fibre R_F. Three types of fibres were designed. A High frequency fibre (HF) with λ=6 mm, A = 3 mm, r_f=0.8 mm; a mid frequency fibre (MF), with λ=10 mm, A = 3 mm, r_f=0.8 mm; and a low frequency fibre with λ=20 mm, A = 3 mm, r_f=0.8 mm. PLA fibres were initially printed as reinforcement into Elk01 material and tested in uni-axial tension and later replaced by more flexible TPU fibres. 2 print layers (0.8 mm + tolerance (0.1 mm)) were used to create the final fibre stls. The 3 stl files were combined and the fibre stl was boolean subtracted from all other components to create a cavity within the gyroid stl, the negative space and the dogbone structure. This allowed for the creation of both the base material's gyroid infill structure, equivalent to approximately 30 % of internal sample volume, and the negative space volume, for the fluid filler, as separate stl files. This further enabled multi-material slicing using Prusa Slicer. The samples were labelled based on their constituents. G30 samples referred to 3 samples prepared with only the 30 % 'empty' gyroid infill. G30Fib refers to 3 samples with a single fibre reinforcement, layered centrally in a gyroid structure. G30Flu refers to samples with PDMS oil as a fluid filler in the negative space of a similar G30 structure, whilst G30FibFlu contains both fibre reinforcement and fluid filler components.

Table 1
Produced material sample acronyms and description.

Designation	Specimen Description		
	Composition	Fibre	Design Parameters
PM	Porcine muscle	N/A	N/A
PL	Porcine liver	N/A	N/A
Elk04	Elkem AMSil20104	N/A	N/A
Elk03	Elkem AMSil20103	N/A	N/A
Elk02	Elkem AMSil20102	N/A	N/A
Elk01	Elkem AMSil20101	N/A	N/A
Elk01HF	Elk01 + high-frequency fibre	PLA	λ=6, A = 3, r_f=0.8 mm
Elk01MF	Elk01 + mid-frequency fibre	PLA	λ=10, A = 3, r_f=0.8 mm
Elk01LF	Elk01 + low-frequency fibre	PLA	λ=20, A = 3, r_f=0.8 mm
G30	Elk01 with infill pattern	N/A	30 % gyroid pattern
G30Flu	G30 + fluid filler	N/A	30 % gyroid + Silicone Oil
G30Fib	G30 + LF fibre	TPU	λ=20, A = 3, r_f=0.8 mm
G30FibFlu	G30 + LF fibre + fluid filler	TPU	λ=20, A = 3, r_f=0.8 mm

2.3. Mechanical testing and analyses

2.3.1. Test protocol

Experiments were carried out using an electro-mechanical test machine (Zwickiline Z030, Zwick Roell GmbH, Ulm, Germany) operated at 10 Hz sampling rate. A high resolution camera (Sony α−6400, Sony, Tokyo Japan) was used for optical video recording at 1 Hz.

White dot markers (GOM, Braunschweig, Germany) were placed slightly below the upper clamped region and above 15 mm from the bottom to avoid bell ends and ensure that the gauge area was vertical (see Fig. 2A). These were used for optical strain tracking analysis with a point tracking algorithm described previously by Frank et al. [58]. Specimens were subsequently clamped on both ends (see Fig. 2C).

Displacement-controlled, uniaxial tensile, triangular wave cyclic loading was applied at 1 mm/s with a preload of 5 mm on the samples with target strain levels (7.5 %, 15.0 %, 25 % and 30 % strain). Each strain level was cycled 8 times to ensure a steady state, the final cycles of each strain level were used to determine the hysteresis (see Fig. 2E).

2.3.2. Suture retention tests

Additionally, suture retention experiments were performed on porcine liver tissue as well as on 3D printed silicone samples to assess the ability of the materials to hold sutures. For suture retention tests, rectangular samples were clamped on one end with a suture material pulled through a notch on the free edge. The notch is created with a suture needle and hence the notch size is dependent on the needle size. This is referred to as the suture bite. The suture bite depth is the distance from the free edge of the specimen (a_b) that shall amount to 2 mm as per the standard. The suture is tied off and pulled with a speed (v) of 1 mm/s. Coated vicryl (polyglactin 910), dyed, braided sutures (Ethicon, New Jersey, USA) were used. Suture bite size of 3 mm was made with a 1/2 circle (rounded) tapered needle. Suture thread thickness was 3 mm and suture length 70 cm (see Fig. 3). The specimens were tested with displacement controlled tensile pull test. The breaking start strength (BSS) as well as the suture retention strength (SRS) were measured and reported.

2.3.3. Stress and strain determination

Actual sample strains were obtained via digital image correlation (DIC). Hereby, the position of the markers is tracked over time and the

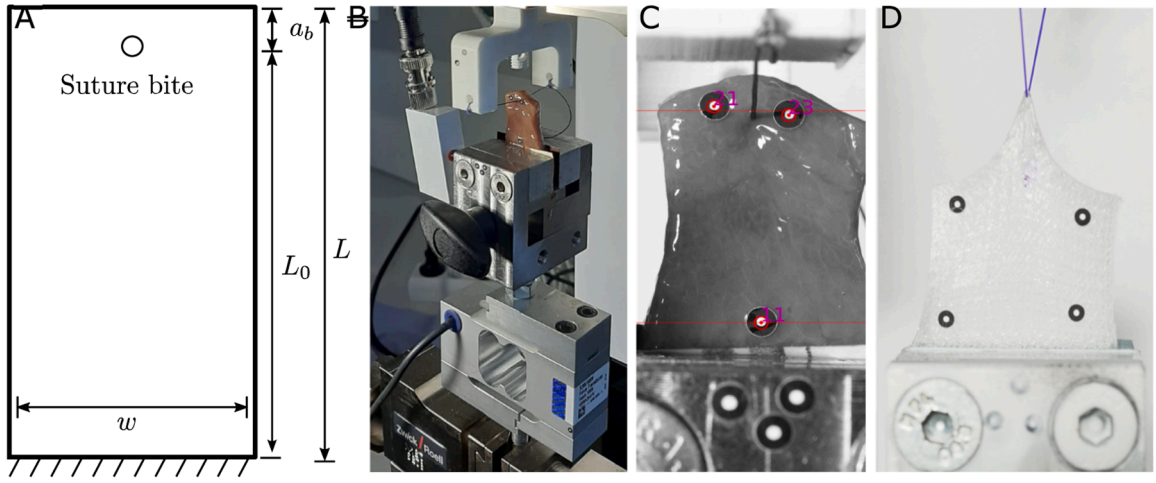

Fig. 3. A) Suture retention test geometry showing suture bite depth (a_o), distance to clamp (L_o) and width(w) B) Mechanical test setup for suture retention C) Porcine liver tissue suture retention test setup showing DIC tracking D) 3D printed silicone sample under suture testing.

relative displacement between the marker positions at the top and bottom is determined. Hence, engineering strain is computed as:

$$\varepsilon(t) = \frac{l(t) - l_0}{l_0} \tag{1}$$

where l_0 is the initial length (at zero-force) and $l(t)$ the actual length of the tissue.

Determination of stiffness. The uni-axial linear engineering stress (σ) is calculated from the axial measured force (f) and the cross sectional area ($A_0 = B \cdot T$), measured with a calliper (prior to testing) and averaged at 3 positions, using the following equation:

$$\sigma(t) = \frac{f(t)}{A_0} \tag{2}$$

The samples were tested in a cyclic manner and the non-linear elastic behavior was analyzed based on the initial and final Young's moduli values at the start and end regions of the material behaviour E and the inflection strain region ε_i (see Fig. 2E).

Determination of energy dissipation. The dissipated energy ratio U_D was calculated as done previously by Aryeetey et al. [47]. The total energy W_T of the triangular wave cycle is the area under the loading half cycle i. e. area ($X + Y$) in Fig. 2E), while the storage energy i.e. elastic energy W_S is the area under the unloading half cycle, i.e. area Y in Fig. 2E. The dissipated energy W_D is the area between the loading and unloading half cycles, area X. The dissipated energy ratio, U_D as defined by Oyen et al. [59] is given by:

$$U_D = \frac{W_T - W_s}{W_T} = \frac{(X+Y) - Y}{(X+Y)} = \frac{W_D}{W_T} \tag{3}$$

2.3.4. Data representation

The material parameters measured E_I, E_{II} and U_D for each specimen type were obtained individually for all 3 samples of the specimen type. For each specimen type, the mean value of the 3 samples were obtained as well as the standard deviation over the 3 samples.

3. Results

3.1. Non-linear elasticity

3.1.1. Base material selection

Porcine muscle and liver tissue both showed the typical non-linear elastic material behaviour of soft collagenous tissues. Porcine muscle tissue showed a mean stiffness E_I of 10±4.0 kPa within the 3 % to 5 % strain range with an increase to a mean final stiffness E_{II} of 580 ± 150 kPa between 15 % to 25 % strain range. Similarly, porcine liver tissue showed an initial stiffness E_I of 3.0 ± 1.0 kPa with a final stiffness E_{II} of 38±21 kPa (see Fig. 3A).

All 3D printed base materials (Elk01 - Elk04) displayed a linear elastic response. The initial and final stiffnesses were relatively similar mostly showing a slight decrease in the final stiffness (see Fig. 3B). The Elk01 material showed the lowest stiffness (140±21 kPa), closest to the chosen soft biological materials and was therefore selected for further testing and tuning. Details of all stiffness results are reported in Table 2. The elastic moduli E_I, E_{II} of all tested samples are exhibited in Fig. 5.

3.1.2. Effect of fibre reinforcement on elastic behaviour

The effect of the fibre reinforcement design was evaluated based on the results of the non-linear response in terms of initial and final elastic modulus E_I and E_{II} and inflection strain ε_i. The fibre reinforcement with varying wavelengths were tested with the aim to result in a strain stiffening behaviour. Only the low-frequency fibre sample (Elk01LF) accomplished this behaviour, whereas the mid- and high-frequency fibre sample still indicated a strain softening behaviour, similar to the bulk material (see Fig. 4 and Table 2). There was no clear inflection in the high-frequency sample, and an inflection at 12 % and 15 % was observed for the mid- and low-frequency samples, respectively.

The non-linear elastic response of Elk01LF was similar to that of porcine muscle tissue, however with a higher initial stiffness E_I of 350 ±20 kPa but a similar final Elastic modulus E_{II} of 520±50 kPa. Further, initial stiffness E_I was increased in all fibre reinforced samples, with respect to the bulk Elk01 material. Taken together, the low-frequency wave design parameters showed the most promising results in terms of non-linear behaviour and inflection strain ε_i and were hence

Table 2
Mean Initial and final elastic moduli ± standard deviation for soft biological tissue, Elkem base silicone samples and fibred samples.

	Muscle	Liver		
E_I	10 ± 4.0	3 ± 1.0		
EII	580 ± 150	38±21		
	ElkHF	ElkMF	ElkLF	
E_I /kPa	260 ± 20	330±30	350 ± 30	
EII /kPa	180±40	240±30	520±50	
	Elk01	Elk02	Elk03	Elk04
E_I /kPa	140 ± 20	780±60	860±80	1900 ± 70
EII /kPa	175 ± 30	520±40	690±90	1800 ± 50

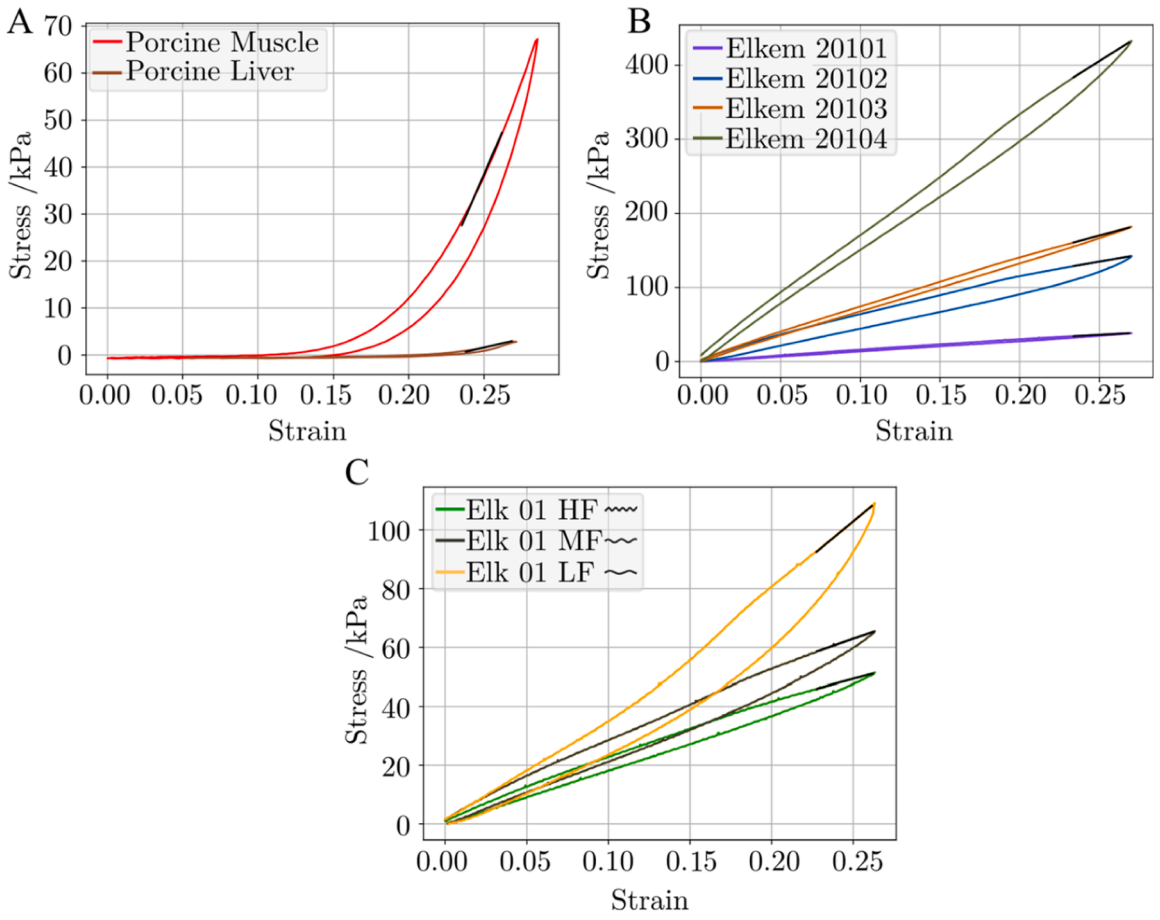

Fig. 4. Selected stress strain plots showing the material behaviour of A) porcine muscle and liver tissue. B) Base silicones Elkem 20,101- Elkem20104 3D printable base materials. C) Fibred Elk01 samples with sinusoidal fibres of high-, mid- and lowfrequency (HF, MF, LF).

implemented in final samples G30Fib and G30FibFlu.

3.1.3. *Effect of gyroid pattern and fluid infill on elastic behaviour*

Fig. 6 shows the stress strain response of Elk01 base silicone, Elk01 with 30 % gyroid infill pattern (G30), and Elk01 with PDMS Oil as a fluid filler (G30Flu), as well as porcine muscle and porcine liver tissue. Reducing the infill percentage from 100 % in Elk01 to G30 sample showed a reduction in initial modulus E_I from 140±30 kPa to 110±10 kPa as well as in the final elastic modulus E_{II} from 175 ± 20 kPa to 80 ±30 kPa. Adding PDMS oil (G30Flu) increased E_I to 250±30 kPa and E_{II} to 190±60 kPa, still lower than the base material Elk01 (see Table 3).

G30Fib showed an initial Elastic modulus E_I of 780 ± 20 kPa and final elastic modulus E_{II} of 970±70 kPa at 12 % strain with the inflection strain ε_i at ≈ 7 % (see Table 3).

Adding the PDMS oil to the fibre reinforced gyroid samples (G30FibFlu) still demonstrated an inflection strain ε_i of ≈ 7 %. Initial and final stiffness was lowered to 510±10 kPa and 400±20 kPa, respectively (see Table 3 and Fig. 4 for an overall comparison of all samples.

Testing performed on fibre reinforced samples displayed characteristics of damage during cyclic testing for cycles with strain levels above 14 % strain. The observed delamination occurred at the clamping regions (see Fig. 9). Results for cycles below this threshold were therefore reported.

3.2. *Suture retention tests*

Additional suture retention tests were performed primarily on porcine liver tissue and 3D printed Elk01 samples with 30 % gyroid infill to assess the capability for anatomical models. For porcine liver tissue, an early failure point (BSS) was observed. The mean BSS over 3 tested samples were determined to be 0.71±0.08 N. The mean suture retention strength of porcine liver tissue measured over 3 samples was 1.64±0.42 N, while for 3D printed silicone samples showed a mean suture retention strength of 5.1 ± 0.6 N with no obvious early failure point observed. Representative samples were selected and are shown in Fig. 7.

3.3. *Dissipated energy ratio*

3.3.1. *Material selection*

The dissipated energy ratio of the various samples was calculated as described in the methods section Equation III. Base materials showed varying hysteresis behaviour based on their chemical composition. Elk01, Elk03, and Elk04 showed relatively low energy dissipation with U_D of 0.09±0.01 and 0.05±0.02, and 0.06±0.01, respectively (see Fig. 6 and Table 4). Elk02 showed higher energy dissipation with 0.21±0.02 much like porcine muscle and liver tissue samples. Elk02 was however not selected for further tuning due to the higher initial stiffness range. Further, as already demonstrated in Fig. 3, the selected base material Elk01 and applied elastic tuning concept Elk01LF already indicated a similar energy dissipation ratio to biological tissue (see also Fig. 6), hence was selected for further material tuning.

3.3.2. *Effect of fluid filler*

The Elk01 with ‘empty’ 30 % gyroid infill (G30) was compared initially to the 100 % filled Elk01 samples and showed an increase in the dissipated energy ratio UD from 0.09±0.01 to 0.16±0.03. The samples filled with PDMS Oil (G30Flu samples) were observed to have an even

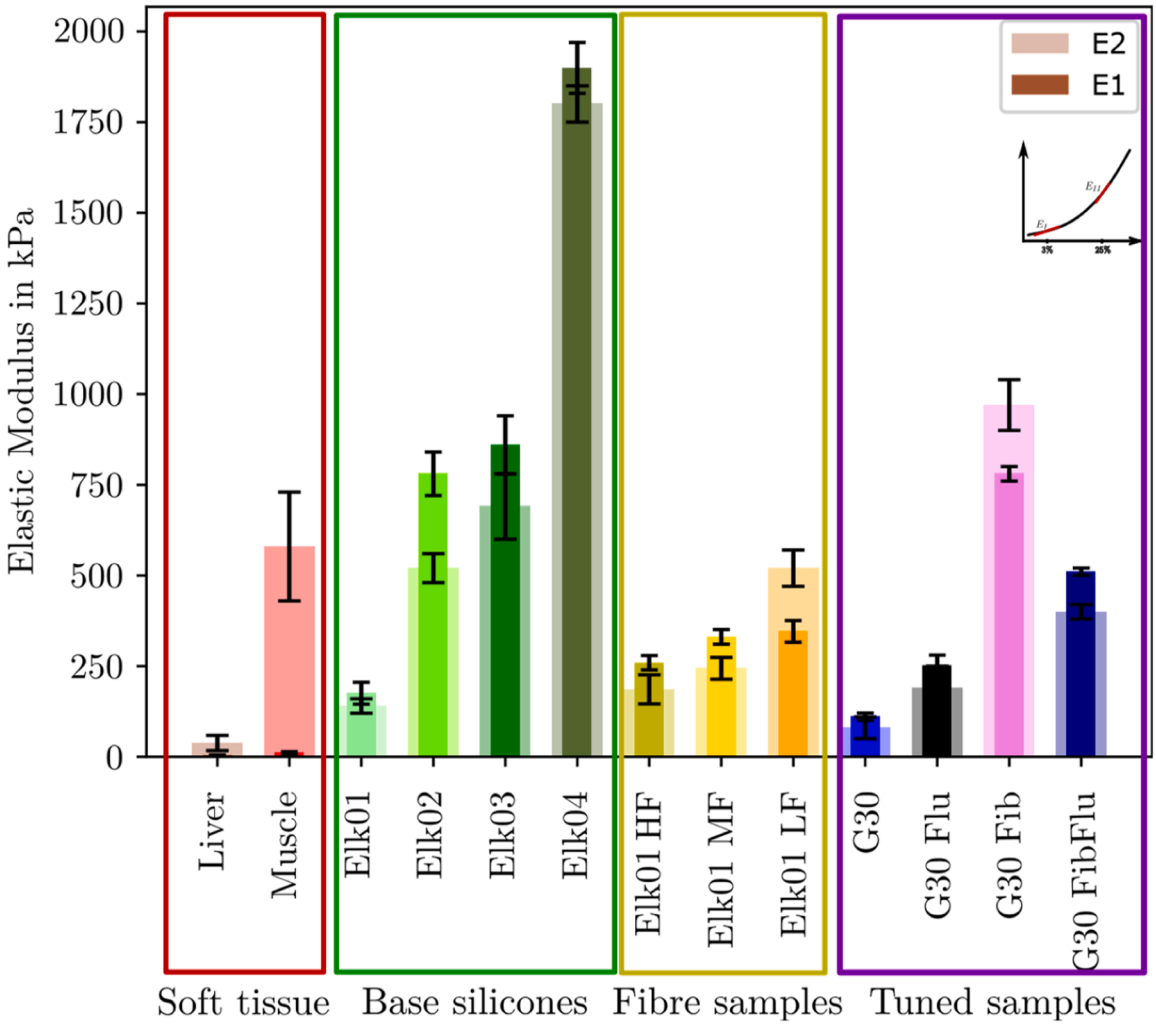

Fig. 5. Initial mean Elastic modulus E_I (darker shade) and final mean Elastic moduli E_{II} (lighter shade) with standard deviation of 3 tested specimens per specimen concept.

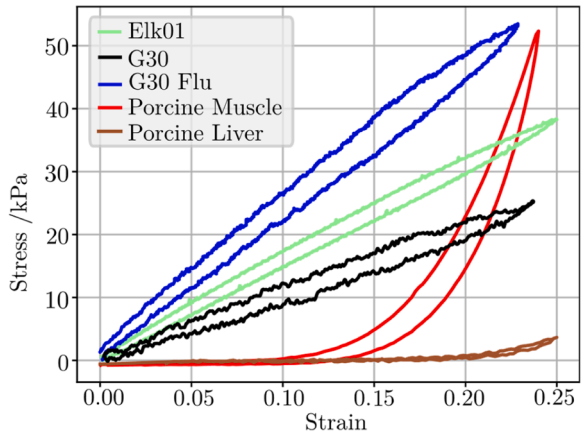

Fig. 6. Stress strain plot of Elkem 20,101 base silicone (Elk01) in green, Elkem 20,101 with 30 % gyroid infill pattern (G30) in black, and Elkem 20,101 base material with PDMS Oil as a fluid filler (G30Flu) in blue as well as porcine muscle and porcine liver tissue in red and brown respectively.

further increase in U_D to 0.23±0.05. These results are like dissipated energy ratio results obtained from porcine muscle tissue of 0.24±0.04.

U_D of the samples are measured at the 8th and final cycle of the triangular wave excitation per strain level. The values are compiled over all 3 specimens of a sample type and box plots (see Fig. 8) show the spread of the results per specimen type. The dissipated energy ratio U_D for the tuned sample G30Fib showed an increase to 0.31±0.03 compared to Elk01, G30, G30Flu. A further increase in U_D is observed with G30FibFlu (0.46±0.17) with the additional component of PDMS oil (see Table 5). Taking a closer look in Fig. 7 demonstrated that samples of G30Fib and G30FibFlu indicated a permanent deformation as stress values become negative after unloading to 0 % strain.

Table 3
Table showing the dissipated energy U_D, mean ± standard deviation for mechanically tuned samples.

	G30	G30Flu	G30Fib @12 %	G30FibFlu @12 %
E_I /kPa	80±30	190 ± 60	970 ± 70	400±20
EII /kPa	110 ± 10	250±30	780±20	510 ± 10

4. Discussion

In this study, extrusion-based 3D printable polymeric materials were tuned to mimic soft biological tissue using a combination of microstructuring, fibre reinforcement and fluid infill and compared to two target soft tissues, porcine liver and porcine muscle tissue.

Results of the final elastic moduli E_{II} of porcine liver tissue (38±21

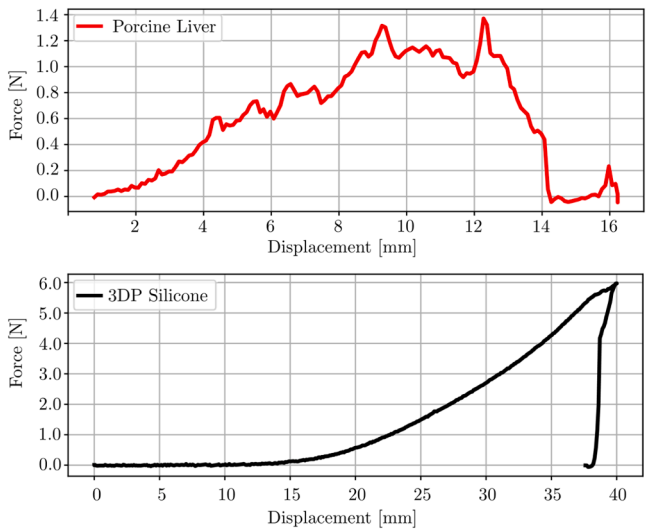

Fig. 7. Representative force-displacement results of suture retention test in porcine liver tissue (top) and 3D printed Elk01 with 30 % gyroid infill (bottom).

Table 4
Mean dissipated energy ratio U_D ± standard deviation for biological tissue, Elkem base silicone samples and fibred samples.

	Muscle	Liver		
U_D	0.24 ± 0.04	0.15 ± 0.12		
	ElkHF	ElkMF	ElkLF	
U_D	0.11 ± 0.02	0.16 ± 0.02	0.17 ± 0.05	
	Elk01	Elk02	Elk03	Elk04
U_D	0.09 ± 0.01	0.21 ± 0.02	0.06 ± 0.01	0.05 ± 0.02

kPa) in our study fall within the range of values reported in literature previously [29,47,60]. Porcine muscle elastic moduli values reported in our study (580 ± 150 kPa), are also within values reported in literature [61,36,62]. Qiu et al. [63] suggests that the range of strains during surgical manipulation is between 0 % and 15 % and hence reported initial E_I and final elastic moduli E_{II} were selected within this range.

Elastic tuning involved the reduction of the elastomers overall stiffness as well as the introduction of non-linear stress stain behaviour in the otherwise linear elastic base material. The chosen base material (Elk01) showed similar stiffness properties to more flexible commercially available print materials flexible materials such as the Tango family from Stratasys, and materials from Ninjatek or PolyFlex, with elastic moduli within the range of 102 kPa and 104 kPa [64–67]. The introduction of a gyroid microstructure to the base Elk01 base material reduced the materials overall final stiffness from 175 ± 30 kPa to 110 ± 10 kPa as hypothesized. This is mainly due to the reduction in the sample's density. Sinusoidal wave fibres (PLA and TPU) were printed into the polymeric matrix and successfully introduced a non-linear elastic behaviour to the sample. As expected, the mismatch of silicone matrix and fibre stiffness introduced an inflection point in the stress strain relationship. The design of the wavy fibre whether high-frequency, mid or low- frequency impacted the inflection strain, while the fibre material affected the stiffness increase after inflection. This concept introduces control to the non-linear stress strain response of polymeric tissue substitutes and hence enables tuning of various materials towards specific collageneous soft tissue. Comparing to previous literature, the strain at the inflection point was higher than those shown by Wang et al. [42] for similar sinusoidal wave fibre reinforcements, which was about 5 %. However, the chosen materials showed a stiffness range of one order of magnitude higher than in those in our study. Garcia et al. [46] also applied similar wavy fibre techniques and successfully introduced non-linear elastic material response for an

Table 5
Table showing the mean dissipated energy U_D ± standard deviation for mechanically tuned samples.

	G30	G30Flu	G30Fib @12 %	G30FibFlu @12 %
U_D	0.16 ± 0.03	0.23 ± 0.05	0.31 ± 0.03	0.46 ± 0.17

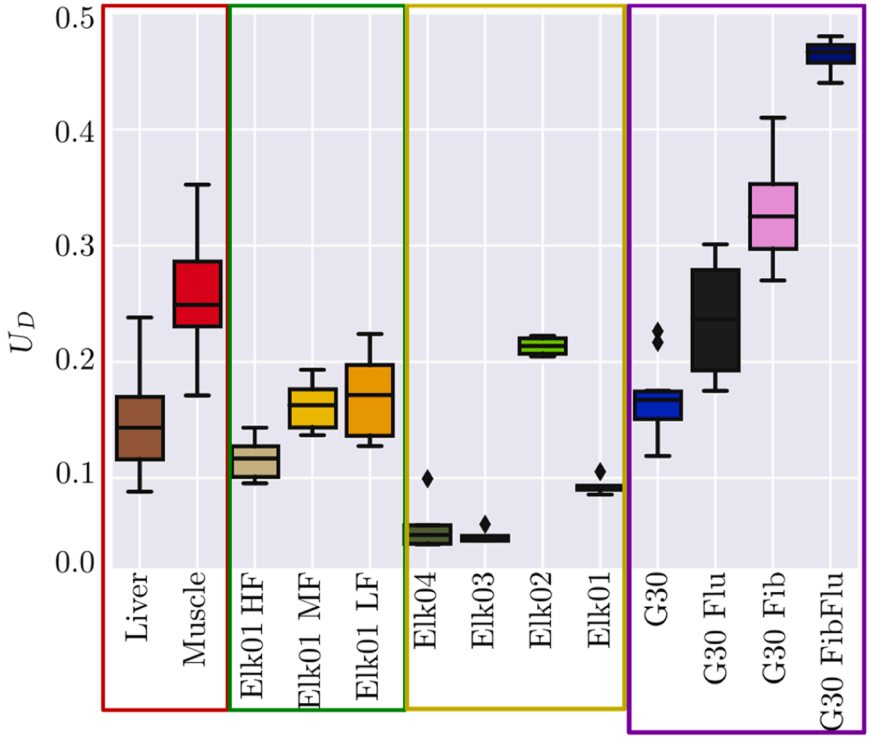

Fig. 8. Boxplots showing the dissipated energy ratio U_D of all materials tested.

ascending aorta model. The stiffness response of designed samples was between 360 kPa and 600 kPa. Hence, our current study was able to mimic soft collagenous tissue in terms of stiffness inflection strain ε_i more realistic.

In terms of viscous tuning, samples with fibre reinforcement also exhibited an increase in the dissipated energy ratio U_D, from the base material value of 0.09 ± 0.01 increasing with fibre frequency from Elk01HF (0.11±0.02), to Elk01LF (0.17±0.05). This is likely attributed to increased energy absorption of stiffening fibres. In accordance, Garcia et al. [46] showed an increase in dissipated energy in the composite fibre-reinforced material (≈ 40 %) as compared to the single Tango Plus material (≈ 35 %). Additionally, it is observed that the introduction of the gyroid microstructure creates an increase in U_D (0.16 ± 0.03). It is hypothesized that the specific infill percentage and distinct pattern of gyroid voids may contribute to energy dissipation within the sample by redistributing stresses or creating zones of localized deformation.

Suture retention tests were performed on both porcine liver tissue and an equivalent G30 sample designed for suture retention tests. Only porcine liver tissue was tested for suture retention as it forms the lower boundary of our experiments and hence is the minimum value for comparison to 3D printed sample. Porcine liver tissue BSS and SRS results were consistent with literature results [68]. Bircher et al. [68] performed suture retention tests on bovine liver tissue and reported a BSS of 1.1 N, consistent with our study of porcine liver tissue (0.71 ± 0.08 N). SRS of the G30 equivalent sample (5.1 ± 0.6 N) was considerably higher than that of porcine tissue (1.64 ± 0.42 N) mainly attributed to the materials higher stiffness properties as compared to soft porcine tissue. Hence, our results show that the 3D printed samples show a sufficient large suture retention strength to withstand manipulation during surgical procedures.

In the present study, the novel concept of introducing a fluid filler (PDMS oil) directly into the sample was used to tune the viscous response. PDMS oil was added as a filler material due to its high viscosity (100 Pas) and showed a further increase in U_D, up to 0.23±0.05. The contribution to the increased dissipated energy ratio was initially attributed to the fluid viscosity. However, the effect of shear thinning behaviour might also contribute to the energy dynamics of the designed tissue samples and should be studied further. The U_D values of our tissue mimicking materials were directly comparable to those of porcine muscle tissue. The final elastic modulus E_{II} of G30Flu sample rose to 190 ±60 kPa, due to an increase in overall sample density, but however did not match that of porcine muscle tissue (580±150 kPa). The G30Fib sample showed an increase in U_D (0.31±0.03) as compared to the G30 (0.16±0.03) and is consistent with the hypothesis that fibre reinforcement increases energy dissipation. The inclusion of PDMS oil i.e. and G30FibFlu samples showed a further increase in U_D (0.46±0.17) attributed to the contribution of both fibre reinforcement and fluid infill to energy dissipation within the sample.

Known limitations of the study are noted. The addition of the PDMS oil to the fibre reinforced gyroid sample showed an unexpected reduction in stiffness (400±20 kPa) as compared to G30Fib (780 ± 20) at the maximum attainable strain at 12 % (see Fig. 9). This is mainly attributed to small leakages of viscous oil during testing around the clamping region. Another limitationwas the damage (partial delamination) occurring in the stress strain plots for strains above 15 % for fibre reinforced G30Fib and G30FibFlu samples. This is attributed to damage of the sample around clamping regions at higher strains, verified by optical inspection after testing. These limitations can be avoided in future studies by increasing the wall thickness of the samples in order to prevent damage to clamping zones. Despite these limitations, the G30FibFlu sample showed an increased viscosityas well as non-linear elastic behaviour in cycles prior to damage cycles as anticipated. The concepts of combining microstructuring, fibre reinforcement and fluid infill to tune tissue mimicking materials mechanical response could thus be clearly demonstrated.

There are several advantages of using such 3D printed phantoms over direct usage of animal samples such as porcine tissue. Firstly, samples are digitally created and are more reproducible, compared to animal soft tissue which likely shows a large variation in mechanical properties (depending on sex, age and species of the animal) [69]. Another major advantage is the ability to further adapt the properties by slight changes in stiffness, non-linear response and energy dissipation as shown in this study for use in other clinical contexts such as in tumor research [20,70]. The use of 3D printed samples can be adapted to use non-toxic substances which are then safer to use as compared to the preparation of samples from animal sources which may contain allergens or pathogens [71]. Additionally, silicone samples can be used for training and testing in any location, while the use of human and animal tissue may be restricted in certain environments.

The results show that it is possible to tune mainly elastic polymeric materials towards soft biological tissues (non-linear elasticity and increased viscosity) within the range of their physiological stresses. Although porcine muscle and liver tissue could not be reproduced exactly, it is shown that the combination of adding fibres and fluid can

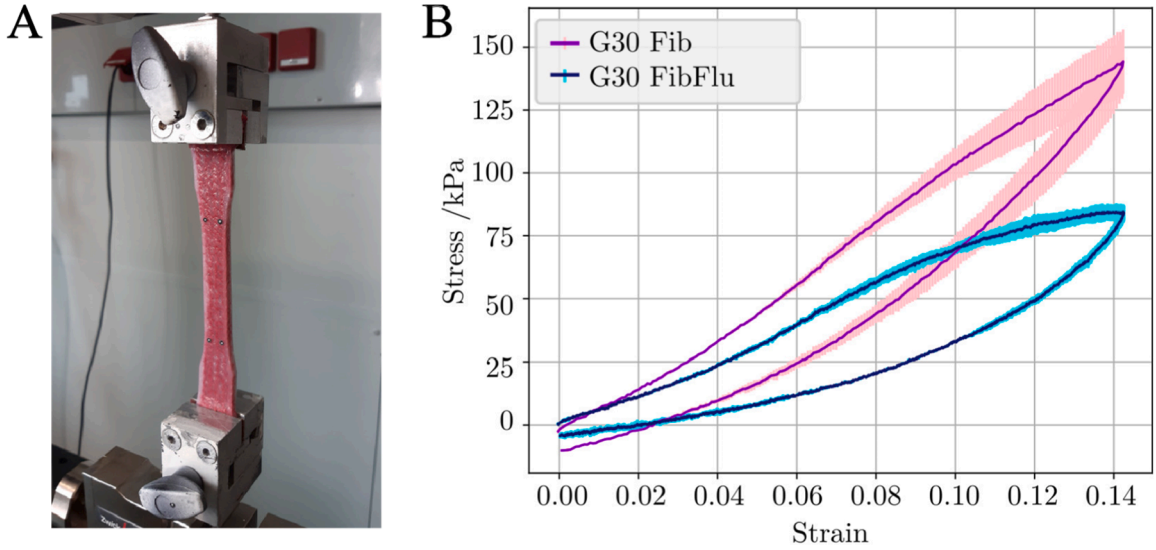

Fig. 9. A) Image of G30FibFlu undergoing uniaxial tensile loading B) Stress strain of samples G30Fib (base material with sinusoidal fibre) and G30FibFlu (base material with sinusoidal fibre and PDMS oil fluid) showing the effect of mechanical tuning with addition of fluid.

be successfully used to tune polymeric base materials close to soft collagenous tissues. Further, the presented mechanisms serve as base tuning concepts that can be further refined and tuned to match a specific tissue by altering the design parameters.

5. Conclusion

This study showed that the mechanical properties, such as non-linear elasticity and viscoelasticity of polymeric base material, can be tuned by combining fibre reinforcement and fluid infill to create tissue mimicking materials. Hereby, a wide range of stiffnesses (80 - 970 kPa) was achieved and energy dissipation of materials was raised by ≈ 40 % using microstructuring and fluid infill. Developed materials also exhibited an adequate suture retention strength (5.1 ± 0.6 N) and hence showed the capacity for use as anatomical phantoms. In future studies, further analysis of infill structures, as well as material properties of viscous fluid infills, will be carried out to create more fine-tuned materials. Also, computational models might be interesting to predict the stress-strain behaviour of those materials to overcome the limitation of physical printing and testing several sets of parameter compositions. Taken together, the basic tools necessary for the development of actual tissue mimicking materials, covering several mechanical aspects at once, have been made available to enable future development of surgical rehearsal anatomical models.

CRediT authorship contribution statement

Othniel James Aryeetey: Formal analysis, Investigation, Methodology, Writing – review & editing, Software, Validation, Visualization, Writing – original draft. **Laszlo Jaksa:** Methodology, Software, Writing – review & editing. **Martin Bittner-Frank:** Supervision, Writing – review & editing. **Andrea Lorenz:** Conceptualization, Project administration, Writing – review & editing. **Dieter H. Pahr:** Writing – review & editing, Conceptualization, Funding acquisition, Supervision.

Declaration of competing interest

The authors declare that they have no known competing financial interests or personal relationships that could have appeared to influence the work reported in this paper.

Acknowledgements

The research was a cooperation with the Austrian Center for Medical Innovation and Technology (ACMIT), funded in the “Forschung, Technologie & Innovation” (FTI) framework of the Provincial Government of Lower Austria (Land Niederösterreich) and funded under grant assignment number WST3F2–528983/005–2018. The authors want to appreciate the contribution of Lower Austria Landesgesundheitsagentur, legal entity of University Hospitals in Lower Austria, for providing the organizational framework to conduct this research. The authors acknowledge TU Wien Bibliothek for financial support through its Open Access Funding Programme.

References

[1] M.A. Makary, M. Daniel, Medical error—the third leading cause of death in the us, BMJ 353 (2016), https://doi.org/10.1136/bmj.i2139.
[2] J.R. Fredieu, J. Kerbo, M. Herron, R. Klatte, M. Cooke, Anatomical models: a digital revolution, Med. Sci. Educ. 25 (2) (2015) 183–194, https://doi.org/10.1007/s40670-015-0115-9.
[3] S. Marconi, E. Negrello, V. Mauri, L. Pugliese, A. Peri, F. Argenti, F. Auricchio, A. Pietrabissa, Toward the improvement of 3d-printed vessels’ anatomical models for robotic surgery training, Int. J. Artif. Organs 42 (2019) 558–565.
[4] K. Qiu, G. Haghiashtiani, M.C. McAlpine, 3d printed organ models for surgical applications, Annu. Rev. Analytical Chem. 11 (1) (2018) 287–306, https://doi.org/10.1146/annurev-anchem-061417-125935.
[5] S.R. Barber, S. Jain, Y.J. Son, E.H. Chang, Virtual functional endoscopic sinus surgery simulation with 3d-printed models for mixed-reality nasal endoscopy, Otolaryngol. Head. Neck. Surg. 159 (5) (2018) 933–937, https://doi.org/10.1177/0194599818797586.
[6] M. Randazzo, J.M. Pisapia, N. Singh, J.P. Thawani, 3d printing in neurosurgery: a systematic review, Surg. Neurol. Int. 7 (Suppl 33) (2016) S801–S809, https://doi.org/10.4103/2152-7806.194059.
[7] Y-xiong Zheng, D-fei Yu, Jian-gang Zhao, Yu-lian Wu, Bin Zheng, 3d printout models vs. 3d-rendered images: which is better for preoperative planning? J. Surg. Educ. 73 (3) (2016) 518–523, https://doi.org/10.1016/j.jsurg.2016.01.003.
[8] K. Wang, C.C. Ho, C. Zhang, B. Wang, A review on the 3d printing of functional structures for medical phantoms and regenerated tissue and organ applications, Engineering 3 (5) (2017) 653–662, https://doi.org/10.1016/J.ENG.2017.05.013.
[9] Z. Jin, Y. Li, K. Yu, L. Liu, J. Fu, X. Yao, A. Zhang, Y. He, 3d printing of physical organ models: recent developments and challenges, Adv. Sci. 8 (17) (2021) 2101394, https://doi.org/10.1002/advs.202101394.
[10] B. Takabi, B.L. Tai, A review of cutting mechanics and modeling techniques for biological materials, Med. Eng. Phys. 45 (2017) 1–14, https://doi.org/10.1016/j.medengphy.2017.04.004.
[11] A. Scerrati, F. Trovalusci, A. Albanese, G.S. Ponticelli, V. Tagliaferri, C.L. Sturiale, M.A. Cavallo, E. Marchese, A workflow to generate physical 3d models of cerebral aneurysms applying open source freeware for cad modeling and 3d printing, Interdiscip. Neurosurg. 17 (2019) 1–6.
[12] M. Wagner, T. Werther, E. Unger, G. Kasprian, G. Dovjak, C. Dorfer, H. Schned, P. Steinbauer, K. Goeral, M. Olischar, K. Roessler, A. Berger, G. Oberoi, Development of a 3d printed patient-specific neonatal brain simulation model using multimodality imaging for perioperative management, Pediatr. Res. 91 (2022) 64–69.
[13] T. Shin, O. Ukimura, I.S. Gill, Three-dimensional printed model of prostate anatomy and targeted biopsy-proven index tumor to facilitate nerve-sparing prostatectomy, Eur. Urol. 69 (2) (2016) 377–379.
[14] Y. Wang, X. Gao, Q. Yang, H. Wang, T. Shi, Y. Chang, C. Xu, Y. Sun, Three-dimensional printing technique assisted cognitive fusion in targeted prostate biopsy, Asian J. Urol. 2 (2015) 214–219.
[15] R.L. Izzo, R.P. O’Hara, V. Iyer, R. Hansen, K.M. Meess, S.V.S. Nagesh, S. Rudin, A. H. Siddiqui, M. Springer, C.N. Ionita, 3d printed cardiac phantom for procedural planning of a transcatheter native mitral valve replacement, in: Proceedings of SPIE–the International Society for Optical Engineering 9789, 2016 978908, https://doi.org/10.1117/12.2216952.
[16] R. Gharleghi, C. Dessalles, R. Lal, S. McCraith, K. Sarathy, N. Jepson, J. Otton, A. Barakat, S. Beier, 3d printing for cardiovascular applications: from end-to-end processes to emerging developments, Ann. Biomed. Eng. 49 (2021).
[17] I. Valverde, G. Gomez, J.F. Coserria, C. Suarez-Mejias, S. Uribe, J. Sotelo, M. N. Velasco, J. Santos De Soto, A.R. Hosseinpour, T. Gomez-Cia, 3d printed models for planning endovascular stenting in transverse aortic arch hypoplasia, Catheteriz. Cardiovasc. Interv. 85 (2015) 1006–1012.
[18] M. Vukicevic, B. Mosadegh, J.K. Min, S.H. Little, Cardiac 3d printing and its future directions, JACC. Cardiovasc. ImAging 10 (2) (2017) 171–184, https://doi.org/10.1016/j.jcmg.2016.12.001.
[19] K.M. Meess, R.L. Izzo, M.L. Dryjski, R.E. Curl, L.M. Harris, M. Springer, A. H. Siddiqui, S. Rudin, C.N. Ionita, 3d printed abdominal aortic aneurysm phantom for image guided surgical planning with a patient specific fenestrated endovascular graft system, Proc. SPIE– Int. Soc. Opt. Eng. (2017) 10138.
[20] C. Hazelaar, M. van Eijnatten, M. Dahele, J. Wolff, T. Forouzanfar, B. Slotman, W.F. A.R. Verbakel, Using 3d printing techniques to create an anthropomorphic thorax phantom for medical imaging purposes, Med. Phys. 45 (2018) 92–100.
[21] G. Doucet, S. Ryan, M. Bartellas, M. Parsons, A. Dubrowski, T. Renouf, Modelling and manufacturing of a 3d printed trachea for cricothyroidotomy simulation, Cureus. 9 (2017) e1575.
[22] I. Hernandez-Giron, J.M. den Harder, G.J. Streekstra, J. Geleijns, W.J. H. Veldkamp, Development of a 3d printed anthropomorphic lung phantom for image quality assessment in ct, Physica Medica 57 (2019) 47–57.
[23] N.N. Zein, I.A. Hanouneh, P.D. Bishop, M. Samaan, B. Eghtesad, C. Quintini, C. Miller, L. Yerian, R. Klatte, Three-dimensional print of a liver for preoperative planning in living donor liver transplantation, Liver Transpl. 19 (2013) 1304–1310.
[24] J.I. Gear, C. Cummings, A.J. Craig, A. Divoli, C.D.C. Long, M. Tapner, G.D. Flux, Abdo-man: a 3d-printed anthropomorphic phantom for validating quantitative sirt, EJNMMI. Phys. 3 (2016) 17.
[25] J. Claflin, S.A. Waits, Three dimensionally printed interactive training model for kidney transplantation, J. Surg. Educ. 77 (2020) 1013–1017.
[26] B. Smith, P. Dasgupta, 3d printing technology and its role in urological training, World J. Urol. 38 (2020) 2385–2391.
[27] Z. Sun, D. Liu, A systematic review of clinical value of three-dimensional printing in renal disease, Quant. ImAging Med. Surg. 8 (3) (2018) 311–325, https://doi.org/10.21037/qims.2018.03.09.
[28] M. Czerner, M. Czerner, L.A. Fasce, J.F. Martucci, R. Ruseckaite, P.M. Frontini, Deformation and fracture behavior of physical gelatin gel systems, Food hydrocolloids v 60 (2016) 299–307, https://doi.org/10.1016/j.foodhyd.2016.04.007.
[29] W. Li, B. Belmont, J.M. Greve, A.B. Manders, B.C. Downey, X. Zhang, Z. Xu, D. Guo, A. Shih, Polyvinyl chloride as a multimodal tissue-mimicking material with tuned mechanical and medical imaging properties, Med. Phys. 43 (10) (2016) 5577–5592, https://doi.org/10.1118/1.4962649.
[30] F. Liu, Q. Chen, C. Liu, Q. Ao, X. Tian, J. Fan, H. Tong, X. Wang, Natural polymers for organ 3d bioprinting, Polymers. (Basel) 10 (11) (2018), https://doi.org/10.3390/polym10111278.

[31] A. Rethy, J.O. Sæternes, J. Halgunset, R. M°arvik, E.F. Hofstad, J.A. Sánchez-Margallo, T. Langø, Anthropomorphic liver phantom with flow for multimodal image-guided liver therapy research and training, Int. J. Comput. Assist. Radiol. Surg. 13 (2018) 61–72.

[32] J. Lim, J. Kim, 3d vascular replicas composed of elastomer-hydrogel skin multilayers for simulation of endovascular intervention, Adv. Funct. Mater. 30 (51) (2020) 2003395, https://doi.org/10.1002/adfm.202003395.

[33] M.M. Maddox, A. Feibus, J. Liu, J. Wang, R. Thomas, J.L. Silberstein, 3dprinted soft-tissue physical models of renal malignancies for individualized surgical simulation: a feasibility study, J. Robot. Surg. 12 (2018) 27–33.

[34] T. Ishii, K. Fukumitsu, E. Ogawa, T. Okamoto, S. Uemoto, Living donor liver transplantation in situs inversus totalis with a patient-specific three-dimensional printed liver model, Pediatr. TransPlant 24 (3) (2020) e13675, https://doi.org/10.1111/petr.13675.

[35] S. Chatelin, J. Oudry, N. Perichon, L. Sandrin, P. Allemann, L. Soler, R. Willinger, In vivo liver tissue mechanical properties by transient elastography: comparison with dynamic mechanical analysis, Biorheology 48 (2011) 75–88.

[36] B. Song, W. Chen, Y. Ge, T. Weerasooriya, Dynamic and quasi-static compressive response of porcine muscle, J. Biomech. 40 (13) (2007) 2999–3005.

[37] M.M. Fitzgerald, K. Bootsma, J.A. Berberich, J.L. Sparks, Tunable stress relaxation behavior of an alginate-polyacrylamide hydrogel: comparison with muscle tissue, Biomacromolecules 16 (5) (2015) 1497–1505, https://doi.org/10.1021/bm501845j.

[38] O.J. Aryeetey, M. Frank, A. Lorenz, S.J. Estermann, A.G. Reisinger, D.H. Pahr, A parameter reduced adaptive quasi-linear viscoelastic model for soft biological tissue in uniaxial tension, J. Mech. Behav. Biomed. Mater. (2021) 104999.

[39] G.D. Goh, S.L. Sing, Y.F. Lim, J.L.J. Thong, Z.K. Peh, S.R. Mogali, W.Y. Yeong, Machine learning for 3d printed multi-materials tissue-mimicking anatomical models, Mater. Des. 211 (2021) 110125.

[40] M. Jaradat, E. Soliman, M.Reda Taha, 3d-printed bio-inspired mechanically interlocked viscoelastic dampers for energy dissipation, Mater. Des. 228 (2023) 111826.

[41] A. Abusabir, M.A. Khan, M. Asif, K.A. Khan, Effect of architected structural members on the viscoelastic response of 3d printed simple cubic lattice structures (2022).

[42] K. Wang, Y. Zhao, Y.H. Chang, Z. Qian, C. Zhang, B. Wang, M.A. Vannan, M. J. Wang, Controlling the mechanical behavior of dual-material 3d printed meta-materials for patient-specific tissue-mimicking phantoms, Mater. Des. 90 (2016) 704–712, https://doi.org/10.1016/j.matdes.2015.11.022.

[43] M. Hao, J. Wang, R. Wang, M. Gong, L. Zhang, D. Wang, Y. Lu, L. Zhang, X. Lin, Mechanical dependence of 3d-printed thermoplastic polyurethane reinforced with minor continuous carbon fibres, Virtual. Phys. Prototyp. 18 (1) (2023) e2224304, https://doi.org/10.1080/17452759.2023.2224304.

[44] S. Wickramasinghe, O. Al-Ketan, C. Peng, Y.L. Tee, M. Kajtaz, P. Tran, Influence of design parameters on the flexural properties of a bio-inspired suture structure, Virtual. Phys. Prototyp. 18 (1) (2023) e2204845, https://doi.org/10.1080/17452759.2023.2204845.

[45] K. Wang, C. Wu, Z. Qian, C. Zhang, B. Wang, M.A. Vannan, Dual-material 3d printed metamaterials with tunable mechanical properties for patient-specific tissue-mimicking phantoms, Addit. Manuf. 12 (2016) 31–37, https://doi.org/10.1016/j.addma.2016.06.006.

[46] J. Garcia, M. AlOmran, A. Emmott, R. Mongrain, K. Lachapelle, R. Leask, Tunable 3d printed multi-material composites to enhance tissue fidelity for surgical simulation, 2018.

[47] O.J. Aryeetey, M. Frank, A. Lorenz, D.H. Pahr, Fracture toughness determination of porcine muscle tissue based on aqlv model derived viscous dissipated energy, J. Mech. Behav. Biomed. Mater. 135 (2022) 105429, https://doi.org/10.1016/j.jmbbm.2022.105429.

[48] T. Finni, J. Peltonen, L. Stenroth, N.J. Cronin, Viewpoint: on the hysteresis in the human achilles tendon, J. Appl. Physiol. 114 (4) (2024) 515–517, https://doi.org/10.1152/japplphysiol.01005.2012.

[49] M. Xi, G. Yun, B. Narsu, A mathematical model for viscoelastic properties of biological soft tissue, Theory Biosci. 141 (1) (2022) 13–25, https://doi.org/10.1007/s12064-021-00361-7.

[50] D. Chimich, N. Shrive, C. Frank, L. Marchuk, R. Bray, Water content alters viscoelastic behaviour of the normal adolescent rabbit medial collateral ligament, J. Biomech. 25 (8) (1992) 831–837, https://doi.org/10.1016/0021-9290(92)90223-N.

[51] L.E. Bilston, Soft tissue rheology and its implications for elastography: challenges and opportunities, NMR Biomed. 31 (10) (2018) e3832, https://doi.org/10.1002/nbm.3832.

[52] Y. Mine, H. Mitsui, Y. Oshima, Y. Noishiki, M. Nakai, S. Sano, Suture retention strength of expanded polytetrafluoroethylene (eptfe) graft, Acta Med. Okayama 64 (2010) 121–128.

[53] S.S. Trostle, D.G. Wilson, W.C. Stone, M.D. Markel, A study of the biomechanical properties of the adult equine linea alba: relationship of tissue bite size and suture material to breaking strength, Vet. Surg. 23 (6) (1994) 435–441, https://doi.org/10.1111/j.1532-950X.1994.tb00504.x.

[54] M. Pensalfini, S. Meneghello, V. Lintas, K. Bircher, A. Ehret, E. Mazza, The suture retention test, revisited and revised, J. Mech. Behav. Biomed. Mater. 77 (2017), https://doi.org/10.1016/j.jmbbm. 2017.08.021.

[55] L. Bernardi, E. Mazza, A.E. Ehret, The effect of clamping conditions on tearing energy estimation for highly stretchable materials, Eng. Fract. Mech. 188 (2017).

[56] L. Jaksa, D. Pahr, G. Kronreif, A. Lorenz, Development of a multi-material 3d printer for functional anatomic models, Int. J. Bioprint. 7 (2021) 420.

[57] L. Jaksa, D. Pahr, G. Kronreif, A. Lorenz, Calibration dependencies and accuracy assessment of a silicone rubber 3d printer, Inventions 7 (2) (2022), https://doi.org/10.3390/inventions7020035.

[58] M. Frank, D. Marx, V. Nedelkovski, J.T. Fischer, D.H. Pahr, P.J. Thurner, Dehydration of individual bovine trabeculae causes transition from ductile to quasi-brittle failure mode, J. Mech. Behav. Biomed. Mater. 87 (2018) 296–305.

[59] M. Oyen, R. Cook, Technique for estimating fracture resistance of cultured neocartilage, J. Mater. Sci. Mater. Med. 12 (2001) 327–332.

[60] A. Nava, E. Mazza, M. Furrer, P. Villiger, W.H. Reinhart, In vivo mechanical characterization of human liver, Med. Image Anal. 12 (2) (2008) 203–216.

[61] C. Van Sligtenhorst, D.S. Cronin, G.Wayne Brodland, High strain rate compressive properties of bovine muscle tissue determined using a split hopkinson bar apparatus, J. Biomech. 39 (2006) 1852–1858.

[62] X. Nie, J.I. Cheng, W.W. Chen, T. Weerasooriya, Dynamic tensile response of porcine muscle, J. Appl. Mech. 78 (2) (2010), https://doi.org/10.1115/1.4002580.

[63] K. Qiu, Z. Zhao, G. Haghiashtiani, S.Z. Guo, M. He, R. Su, Z. Zhu, D.B. Bhuiyan, P. Murugan, F. Meng, S.H. Park, C.C. Chu, B.M. Ogle, D.A. Saltzman, B.R. Konety, R.M. Sweet, M.C. McAlpine, 3d printed organ models with physical properties of tissue and integrated sensors, Adv. Mater. Technol. 3 (3) (2018) 1700235, https://doi.org/10.1002/admt.201700235.

[64] S.J. Yoo, T. Spray, E.H.r. Austin, T.J. Yun, G.S. van Arsdell, Handson surgical training of congenital heart surgery using 3-dimensional print models, J. Thorac. Cardiovasc. Surg. 153 (2017) 1530–1540.

[65] L. Kiraly, M. Tofeig, N.K. Jha, H. Talo, Three-dimensional printed prototypes refine the anatomy of post-modified norwood-1 complex aortic arch obstruction and allow presurgical simulation of the repair, Interact. Cardiovasc. Thorac. Surg. 22 (2016) 238–240.

[66] S.N. Kurenov, C. Ionita, D. Sammons, T.L. Demmy, Three-dimensional printing to facilitate anatomic study, device development, simulation, and planning in thoracic surgery, J. Thorac. Cardiovasc. Surg. 149 (2015) 973–979.

[67] S. Bustamante, S. Bose, P. Bishop, R. Klatte, F. Norris, Novel application of rapid prototyping for simulation of bronchoscopic anatomy, J. Cardiothorac. Vasc. Anesth. 28 (2014) 1122–1125.

[68] K. Bircher, M. Zündel, M. Pensalfini, A.E. Ehret, E. Mazza, Tear resistance of soft collagenous tissues, Nat. Commun. 10 (1) (2019) 792, https://doi.org/10.1038/s41467-019-08723-y.

[69] G.A.I. Arroyave, R.G. Lima, P.A.L.S. Martins, N. Ramīao, R.M.N. Jorge, Methodology for mechanical characterization of soft biological tissues: arteries, Procedia Eng. 110 (2015) 74–81.

[70] R. Cao, Z. Huang, T. Varghese, G. Nabi, Tissue mimicking materials for the detection of prostate cancer using shear wave elastography: a validation study, Med. Phys. 40 (2013) 022903.

[71] B.H.P. Mobo, P.M. Rabinowitz, L.A. Conti, O.A. Taiwo, Occupational health of animal workers. (2010).